

Tuning crystallization pathways through sequence engineering of biomimetic polymers

Xiang Ma^{1†}, Shuai Zhang¹, Fang Jiao^{1,2}, Christina J. Newcomb¹, Yuliang Zhang³, Arushi Prakash^{1,4}, Zhihao Liao^{1,5}, Marcel D. Baer¹, Christopher J. Mundy^{1,4}, James Pfaendtner^{1,4}, Aleksandr Noy^{3,6}, Chun-Long Chen^{1*} and James J. De Yoreo^{1,7*}

Two-step nucleation pathways in which disordered, amorphous, or dense liquid states precede the appearance of crystalline phases have been reported for a wide range of materials, but the dynamics of such pathways are poorly understood. Moreover, whether these pathways are general features of crystallizing systems or a consequence of system-specific structural details that select for direct versus two-step processes is unknown. Using atomic force microscopy to directly observe crystallization of sequence-defined polymers, we show that crystallization pathways are indeed sequence dependent. When a short hydrophobic region is added to a sequence that directly forms crystalline particles, crystallization instead follows a two-step pathway that begins with the creation of disordered clusters of 10–20 molecules and is characterized by highly non-linear crystallization kinetics in which clusters transform into ordered structures that then enter the growth phase. The results shed new light on non-classical crystallization mechanisms and have implications for the design of self-assembling polymer systems.

In the classical picture of nucleation from solutions, density fluctuations create unstable clusters of the new phase through monomer-by-monomer addition¹. These clusters transition from unstable to stable when they exceed the size beyond which the free energy cost of creating a new phase boundary is overcompensated by a drop in chemical potential. In recent years, hierarchical pathways involving assembly of species more complex than monomers have been proposed for many systems^{2–8}. These pathways include two-step processes, originally hypothesized for proteins^{4,7,8}, by which crystals form within monomer-rich, non-crystalline clusters that appear spontaneously. However, reports of such pathways are primarily based on simulations or indirect measurements^{9,10}, although in limited cases such as colloidal systems¹¹ and protein solutions undergoing phase separation^{2,4} direct observations have been reported. Moreover, the dynamics of two-step pathways are poorly understood: whether monomers in the clusters produce the first crystalline particle or instead provide an environment for heterogeneous nucleation is uncertain. The degree to which pathways depend upon the details of molecular structure and whether two-step processes are general features of macromolecular systems is also unknown. Here we exploit the sub-nanometre resolution of atomic force microscopy (AFM) and the propensity of surfaces to promote crystallization to observe pathways for biomimetic polymers forming two-dimensional crystalline sheets and porous networks.

Polymer design and crystallization

Twelve residue biomimetic polymers called peptoids¹² were synthesized with two distinct sequences that alternated between

(hydrophilic) carboxyl and (hydrophobic) chlorophenethyl side chains (Fig. 1a,b) (Methods, Supplementary Methods, part I and Supplementary Figs 1 and 2). In one of these—Pep_c—a hydrophobic region was conjugated to the final carboxyl residue of the basic sequence—Pep_b. When mixed with CaCl₂ solutions and incubated with freshly cleaved mica substrates, both peptoids assembled into three-dimensional porous networks (Fig. 2a,f). Images collected at earlier times showed these networks began as arrays of 5-nm-wide linear structures, 3.3 nm in height, that grew outwards to form vertically oriented sheets aligned along three directions, each separated by 120° (Fig. 2e,j).

The molecular structure of the sheets could not be directly determined by X-ray diffraction (XRD) due to strong diffraction from the substrate, but based on peptoid dimensions and XRD data from similar peptoids (Supplementary Fig. 3)^{13–15}, we conclude the sheets are crystalline and consist of stacks of bilayers, one peptoid in width with the chlorophenethyl groups facing towards the centre of each bilayer (Fig. 1c), consistent with previous reports of sheet-forming peptoids^{13–15}. Because the pK_a of the peptoids is well below the neutral pH of the experiments (for example, pK_a of Pep_c = 5.1), all carboxyl groups are fully deprotonated and the Ca²⁺ ions serve to bridge bilayers through Ca²⁺–carboxylate interactions¹⁶. Due to spontaneous substitution of Ca²⁺ into the K⁺ surface sites of mica^{17,18}, the addition of Ca²⁺ served to template growth of fibres and sheets into the three-fold symmetric pattern. Demonstration of this relationship was obtained by imaging mica at atomic resolution before forming the three-fold arrays, and comparing orientations of peptoid crystals to the structure of the

¹Physical Sciences Division, Pacific Northwest National Laboratory, Richland, Washington 99352, USA. ²School of Chemistry and Molecular Engineering, East China Normal University, Shanghai 200241, China. ³Physical and Life Sciences Directorate, Lawrence Livermore National Laboratory, Livermore, California 94550, USA. ⁴Department of Chemical Engineering, University of Washington, Seattle, Washington 98195, USA. ⁵Center for Biomaterials and Biopathways, Department of Chemistry, Zhejiang University, Hangzhou, Zhejiang 310027, China. ⁶School of Natural Sciences University of California Merced, Merced, California 95343, USA. ⁷Department of Materials Science and Engineering, University of Washington, Seattle, Washington 98195, USA.

[†]Present address: Department of Chemistry, Idaho State University, Pocatello, Idaho 83201, USA. *e-mail: chunlong.chen@pnnl.gov; james.deyoreo@pnnl.gov

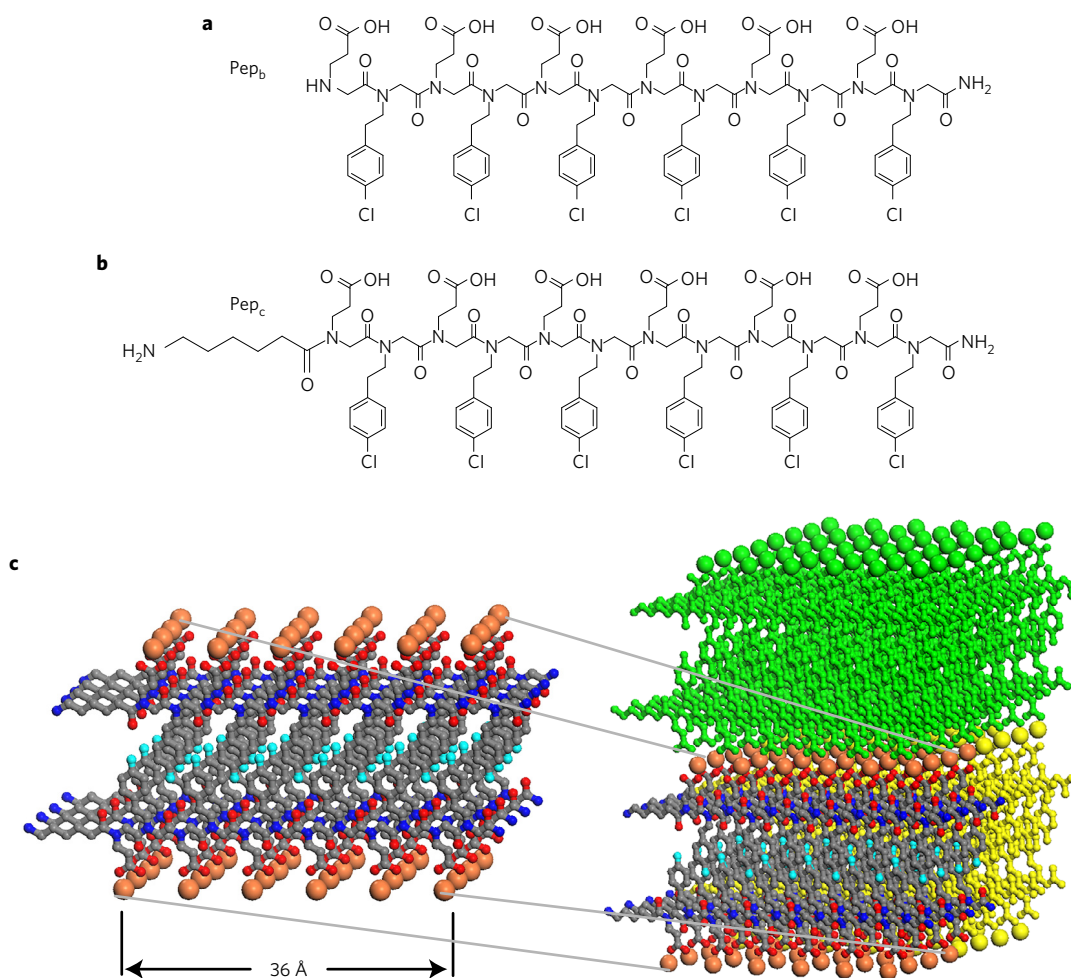


Figure 1 | Structures of peptoid molecules and crystals formed on mica. **a, b**, Molecular structures of Pep_c (**a**) and Pep_b (**b**). **c**, The proposed model showing fully deprotonated Pep_c assemblies of linear bilayer-like structures combining Ca²⁺–carboxylate coordination bonds and hydrophobic interactions; peptoid fibres grow perpendicularly to the surface. Colour code: C, grey; O, red; N, blue; Cl, cyan; Ca²⁺, orange.

mica surface (Supplementary Fig. 4). The data show the peptoids are aligned at 30° to the three orientations of densest cation packing in the mica lattice. The 9.0 Å distance between cation sites along these directions leads to an epitaxial match of the two end carboxyl groups, which lie 36 Å apart in a linear peptoid model^{13–15}.

Crystallization pathways and kinetics

To determine the mechanism and kinetics of crystallization, we performed *in situ* AFM (Methods) with both sequences from the time of initial mixing of peptoid solution and CaCl₂ buffer until the three-fold arrays were fully formed (Fig. 2b–e,g–j).

The crystallization of Pep_c started with the deposition of ~5-Å-high clusters up to ~15 nm in diameter, which periodically transformed into 3-nm-high particles with an initial length of ~5 nm (Fig. 2b,c). These particles functioned as nuclei for the 3-fold symmetric arrays of vertical sheets (Fig. 1). As each one extended laterally along a single axis to create an initial 3-fold symmetric array of linear features, a second 3-nm-high layer formed on the top surface (Fig. 2c,d). This process continued, leading to the formation of the vertically aligned sheets (Fig. 2e), which grew outwards in 3-nm increments (Fig. 3a) with a gradual loss of symmetry to ultimately form a three-dimensional porous network.

Eliminating the hydrophobic conjugate altered the peptoid crystallization dynamics (Fig. 2g–j). Even in the earliest images, only 3-nm- and 6-nm-high particles of Pep_b were observed and 5-Å-high clusters were absent (Fig. 2g). Subsequent development of

3-fold arrays of vertical sheets and porous networks was similar to that observed for Pep_c, showing incremental growth in 3-nm steps (Fig. 3b), although the rate of vertical growth relative to elongation was much greater. Consequently, the crystals had often reached a height of 6 nm by the time the first image was collected.

The kinetics of crystal formation were determined for a range of peptoid and Ca²⁺ concentrations. For relatively high Pep_c concentrations, the formation rate *J* of 3-nm-high particles transitioned from a low to high value after a time τ that decreased with the increase of both peptoid concentration *C_p* and Ca²⁺ concentration *C_{Ca}* (Fig. 3c). However, at low peptoid concentrations, no such transition was observed, and formation rates remained low (Fig. 3c). After the transition, the rate increased with peptoid concentration but was constant over the range of Ca²⁺ concentrations investigated here. In stark contrast, for Pep_b, formation rates decreased with time in accordance with a simple Langmuir dependence and were dependent on both peptoid and Ca²⁺ concentrations (Fig. 3d).

The number density of the 5-Å-high Pep_c clusters exhibited a dependence that correlated with the number density of 3-nm-high nuclei and revealed a key step in the formation pathway. The value of *J* for 5-Å-high clusters was initially constant and rapid in comparison to that of 3-nm-high nuclei, but their number reached a maximum before rapidly decreasing (Fig. 4a). Analysis of the location of each cluster and nucleus showed that, for all Pep_c and Ca²⁺ concentrations, during the initial (slow) phase of crystal formation, all particles were formed through the transformation

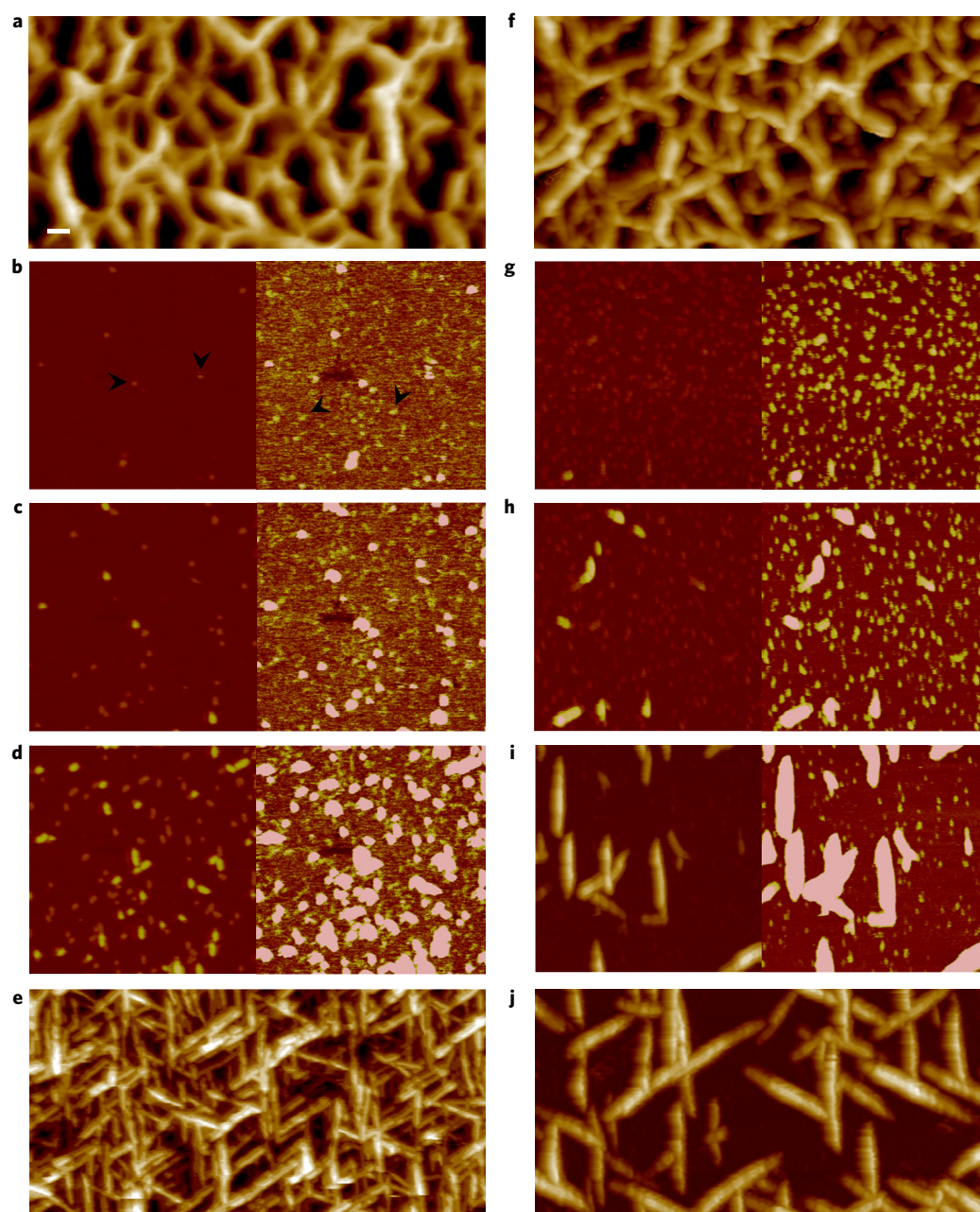


Figure 2 | In situ view of peptoid assembly and resulting morphologies. **a–e**, Crystallization of Pep_c. **f–j**, Crystallization of Pep_b. **a, f**, Ex situ AFM images showing self-assembled porous networks of Pep_c (**a**) and Pep_b (**f**) after two days of incubation. Vertical scale: 67.5 nm. **b–e, g–j**, In situ AFM images showing assembly pathway in 10 mM CaCl₂ solution with 0.1 mM Pep_c at $t = 24.2$ (**b**), 32.3 (**c**), 50.1 (**d**) and 275.1 (**e**) min, and 0.1 mM Pep_b at $t = 4.3$ (**g**), 17.2 (**h**), 69.1 (**i**), and 111.2 (**j**) min. In each image of **b–d** and **g–i**, the left and right panels are presented with different vertical scales (12 nm and 0.8 nm, respectively, for Pep_c (**b–d**); 12 nm and 4 nm, respectively, for Pep_b (**g–i**)), to clearly show the hierarchy of structures. Vertical scale for **e, j** is 12 nm. Arrowheads in **b** indicate nuclei (left panel) and clusters (right panel). Scale bar in **a** is 50 nm and applies to all images.

of pre-existing 5-Å-high clusters (Fig. 4b), which had volumes similar to those of the crystalline nuclei. The coverage of clusters at any given time was so low ($\sim 0.5\%$) that the probability of this transformation corresponding to a random deposition event at the same location was insignificant ($\sim 10^{-3}$). Moreover, the time of the transition to rapid crystal formation coincided with a sudden drop in the percentage of crystals that formed from pre-existing 5-Å-high clusters (Fig. 4b). In other words, this time point marked the onset of an alternate pathway for the creation of Pep_c crystals. In contrast, at low Pep_c concentrations, where no transition to high J was observed, the 5-Å-high clusters were the exclusive source of crystals throughout the experiment. Moreover, when a high (0.1 mM)

concentration Pep_c solution was passed through a 0.2 μm filter prior to imaging, no transition occurred and the kinetics of crystal formation were identical to those seen at ten times lower (0.01 mM) Pep_c concentrations. When that same concentration solution was injected after an initial period of growth in low-concentration solution, the kinetics again exhibited a transition from low to high J after the expected incubation time (Supplementary Fig. 5).

The drop in the number of 5-Å-high clusters, the transition to direct appearance of crystalline particles, and the elimination of that transition through filtration all suggest that Pep_c forms higher-order species in solution immediately upon mixing, and the distribution of these species evolves with time, influencing the availability of

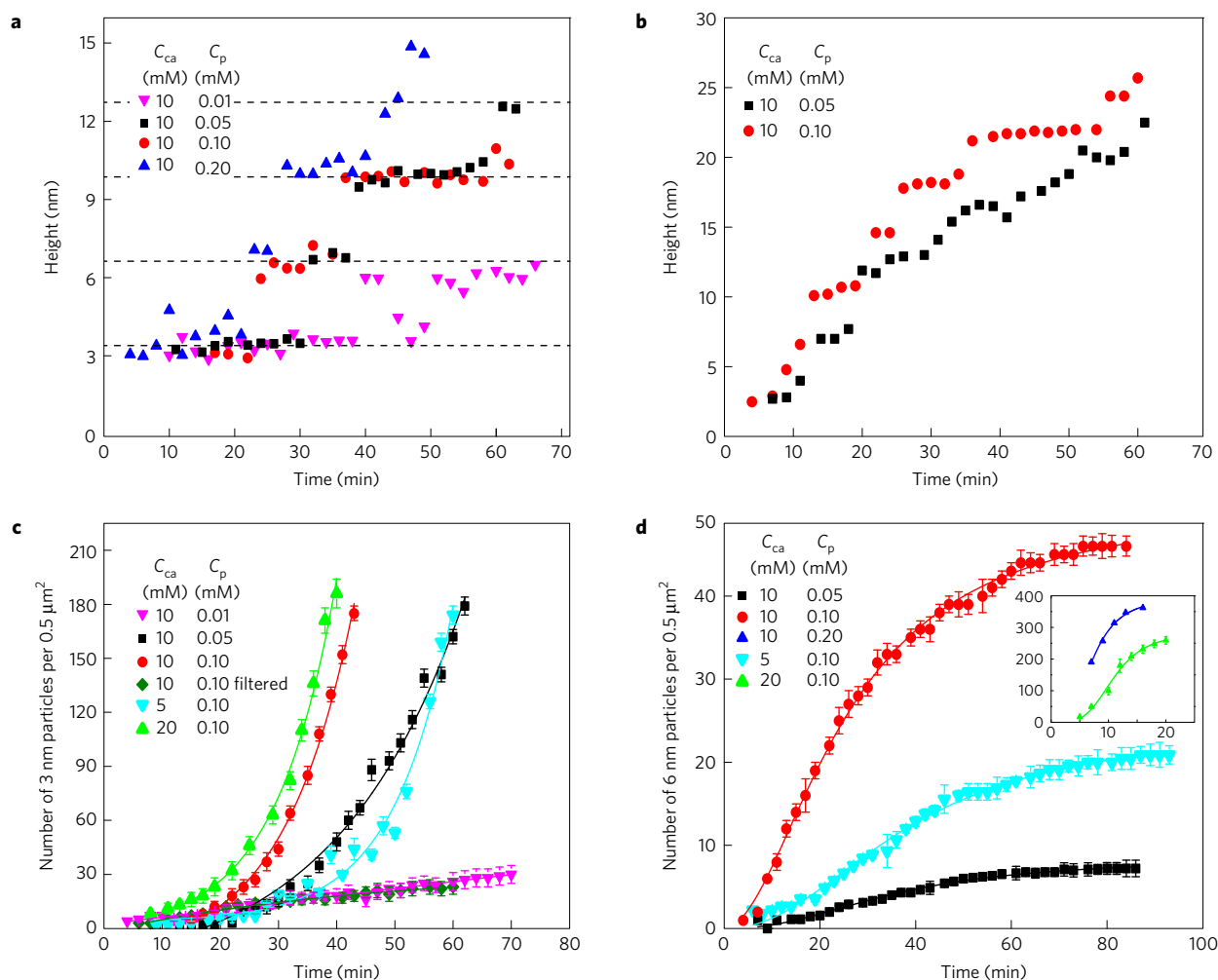


Figure 3 | Kinetics of crystal formation and bilayer addition. **a,b**, Height versus time for Pep_C (**a**) and Pep_B (**b**) in 10 mM CaCl₂ solution. **c,d**, Crystal number density versus time for a range of peptoid and Ca²⁺ concentrations for Pep_C (**c**) and Pep_B (**d**). For the curve marked '10 mM Ca²⁺ 0.1 mM Pep_C filtered', the solution was passed through a 0.2 μm filter immediately after mixing and before injection into the AFM fluid cell. Error bars denote two standard errors (SEs) of the measurements collected at each condition. Solid lines are guides to the eye.

all surface species. Both dynamic light scattering (DLS) and cryogenic transmission electron microscopy (cryo-TEM) experiments confirmed this conclusion. DLS revealed the presence of solution aggregates hundreds of nanometres in diameter immediately after mixing (Supplementary Fig. 6a) and showed that addition of Ca²⁺ increased the average aggregate size (Supplementary Fig. 6b,c). TEM performed on Ca²⁺ containing samples collected immediately after mixing also revealed aggregates hundreds of nanometres in size (Supplementary Fig. 7). Moreover, when solutions were allowed to incubate, a higher concentration of aggregates with a wide range of sizes was observed (Supplementary Fig. 7b,d,e).

Mechanistic model of crystallization

These observations suggest the following model of crystal formation for the two peptoids. Upon mixing of Pep_C solutions, due to the presence of the hydrophobic region, the peptoid monomers aggregate both into small clusters, which are below the limit of resolution of DLS or TEM, and large aggregates, which serve as a reservoir for smaller species. Given the amphiphilic nature of Pep_C, the solution clusters are likely to consist of micelles that form spontaneously in the solution. These deposit on the surface, forming surface clusters in which the molecules are randomly arranged and 'lying down' with a height approximately given by the ~4.5 Å width of a monomer (Fig. 5a). These clusters deposit at a constant rate

and periodically undergo conformational transformations to 'stand up' into crystalline bilayer particles with heights of 3 nm. The crystals then grow through monomer attachment to the ends and the formation of new bilayers on the top. However, the transformation of clusters into the initial crystalline particles eventually begins to take place in solution as well, leading to a decrease in the deposition rate of 5-Å-high clusters and the onset of direct deposition of the 3-nm-high bilayer particles. At very low peptoid concentrations, or following filtration, the peptoid concentration is insufficient to drive crystal formation in solution and no transition occurs. In contrast, upon mixing of Pep_B solutions, monomers readily form crystalline particles in solution, which deposit on the surface at a rate that decreases as coverage increases, as expected for a Langmuir adsorption process. Thus the generation of Pep_C by addition of the extra hydrophobic region to Pep_B alters the formation pathway from a single-step to a two-step process and modifies the corresponding free energy landscape to create a transient microscopic state whose formation and transformation controls the kinetics of crystallization (Fig. 5c).

To test the model of Pep_C crystallization, we solved a set of coupled rate equations that include the processes described above (Supplementary Methods, part II). There are two time (*t*) regimes. For *t* ≤ *τ* (Fig. 5a), the solution contains only disordered clusters, which adsorb onto the surface, and crystalline particles are only

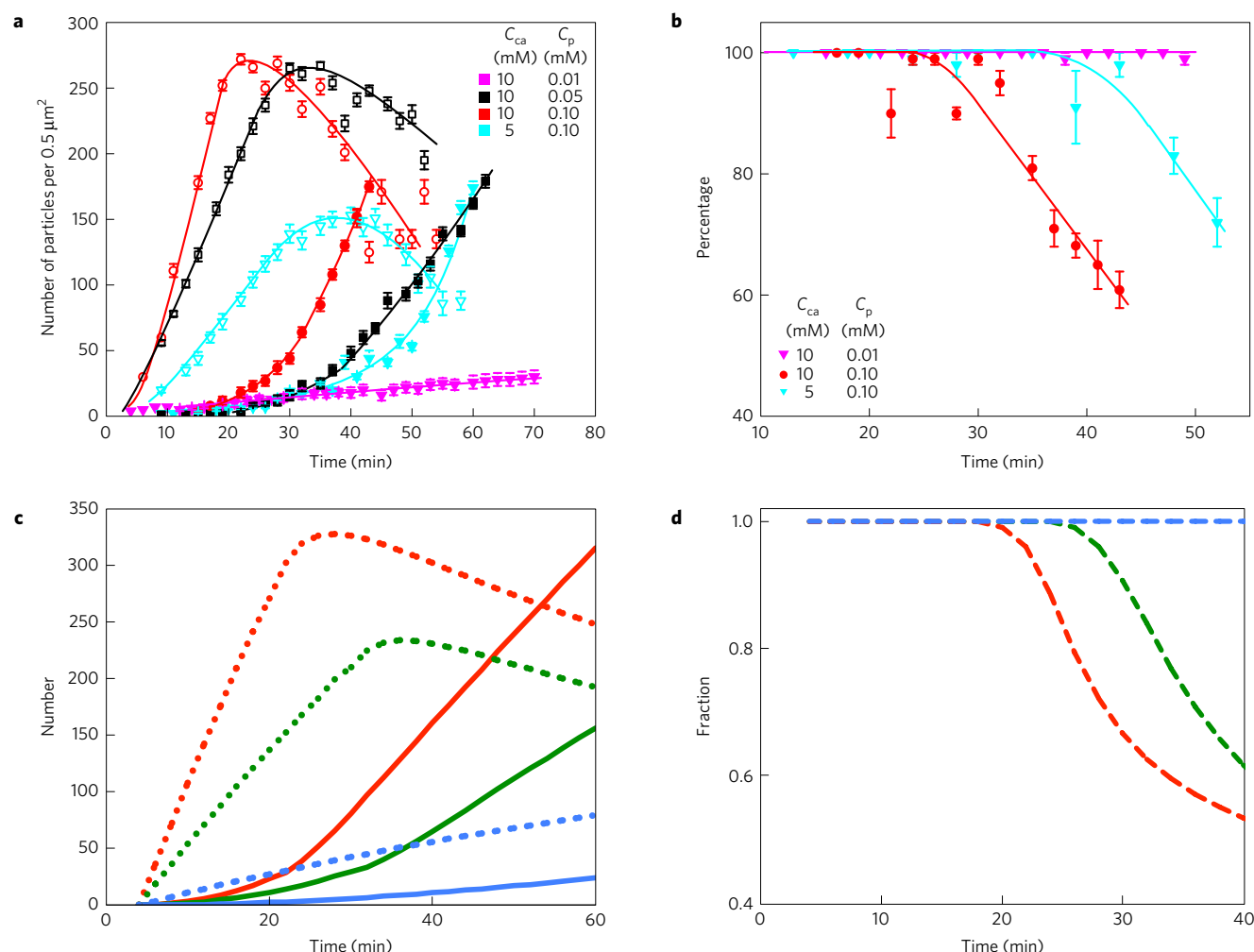


Figure 4 | Comparison of Pep_c cluster and crystal formation rates with model predictions. **a**, Number density of clusters (open symbols) and crystals (closed symbols) versus time. **b**, Percentage of 3-nm-high crystalline particles that transformed from pre-existing 5-Å-high clusters versus time for a range of peptide and Ca²⁺ concentrations. Error bars denote two SEs of the measurements collected at each condition. Solid lines are guides to the eye. **c,d**, Representative model predictions corresponding to **a** and **b**, respectively, where, in **c**, solid lines correspond to crystals and dotted lines to clusters (see text and Supplementary Methods, part II for details of the model). Model parameters $A_{Cl}C_{Cl}^0$, K_{Nu} , T_{Nu} , $(1/m)K_{Nu}C_{Cl}^0$ and τ , where A_{Cl} is the rate constant for cluster adsorption, C_{Cl}^0 is the cluster concentration in solution at time $t=0$, K_{Nu} and T_{Nu} are the rate coefficients for transformation of clusters into crystal nuclei in solution and on the surface, respectively, m is the average number of monomers in a cluster, and τ marks the time when clusters in solution begin to transform into nuclei; all are in units of inverse time (here set to minutes⁻¹). In both **c** and **d** the values are: Red—18.5, 0.25, 0.01, 5, and 17; Green—9.5, 0.25, 0.01, 2.5, and 27; Blue—1.85, 0.25, 0.01, 0.5 and >60.

created by their subsequent transformation. For $t \geq \tau$ (Fig. 5b), crystals are created both by transformation of deposited clusters and by direct deposition of crystalline particles, where the latter begin to form at the expense of solution clusters after time τ .

Representative solutions to the equations (Fig. 4c,d and Supplementary Methods, part II) exhibit all the features observed in the experiments, including the time dependencies, transition times, and magnitudes of the cluster and crystalline particle densities (Fig. 4c), as well as the fraction of crystals that come from transformation of adsorbed clusters (Fig. 4d). The results support the conclusion that the addition of the hydrophobic region leads to a two-step process marked by the formation of precursor clusters that convert into the initial particles of the crystalline sheets.

We used dynamic force spectroscopy (DFS)^{19,20} to relate the decrease in τ and increase in J with increasing C_{Ca} , by determining the free energies for Pep_b–Pep_b binding (ΔG_{P-P}) and Pep_b–mica binding (ΔG_{P-M}) (ref. 19) for different C_{Ca} (Methods). The results show that ΔG_{P-P} and ΔG_{P-M} exhibit opposite dependencies on C_{Ca} , with ΔG_{P-P} decreasing and ΔG_{P-M} increasing with C_{Ca} , respectively

(Table 1 and Supplementary Fig. 8). With the caveat that increasing Ca²⁺ levels may lead to increased binding between peptides on the tip, and thus less binding to the surface, these results provide a rationale for the observed dependence of crystallization kinetics on C_{Ca} . As ΔG_{P-M} increases, the rate of coverage by both clusters and nuclei should rise, thus increasing J . As ΔG_{P-P} decreases, the ability of peptides to reversibly bind and reorganize should also rise, thus reducing τ .

Structural source of pathway switching

Although addition of the hydrophobic region in Pep_c drives formation of disordered clusters, the question remains as to whether the effect is due to hydrophobic interactions or added molecular flexibility. To probe the effect of the added region, we performed molecular dynamics (MD) simulations of Pep_b and Pep_c pairs in water with and without Ca²⁺ (Supplementary Methods, part III). In the absence of Ca²⁺, the potential of mean force (PMF) for Pep_b exhibits no clear minimum and thus no significant dimerization, but addition of Ca²⁺ leads to dimer stabilization through the carboxyl

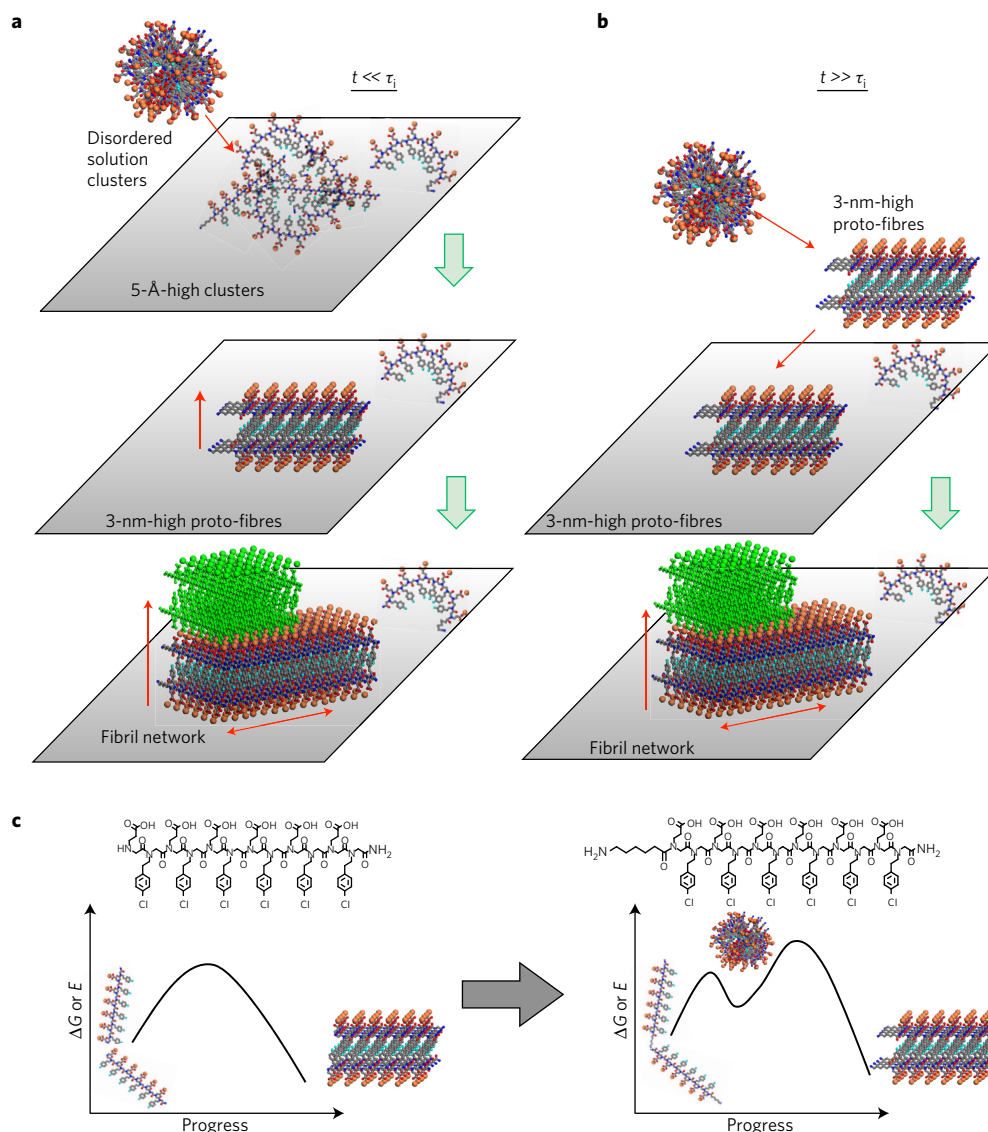


Figure 5 | Proposed peptoid crystallization pathways and energy landscapes. **a, b**, Proposed model for Pep_c assembly process at early (**a**) and late (**b**) stages showing the effect of hydrophobic conjugate on the propensity for peptoid aggregation. **c**, Alteration in pathway from a single step for Pep_b to a two-step process for Pep_c and modification in corresponding energy barriers associated with the addition the hydrophobic region to Pep_b . The colour scheme for the atoms is the same as in Fig. 1.

groups (Supplementary Fig. 9). In contrast, the PMF for Pep_c exhibits no minimum with or without Ca^{2+} ; instead peptoids remain dissociated, with the hydrophobic tail wrapped inwards. These findings highlight the fact that cluster formation due to hydrophobic interactions is a collective phenomenon that requires a large enough number of molecules before stabilization can occur (although a full MD simulation of such a system with ions and explicit waters is not feasible). The results support the conclusion that the hydrophobicity of the added region drives the change in pathway and kinetics in going from Pep_b to Pep_c .

We also examined crystallization of two other peptoids, one in which the hydrophobic tail of Pep_c was replaced with a hydrophilic tail to give Pep_h (Supplementary Fig. 10), and another in which it was replaced with two phenyl rings to give Pep_r , having a similar degree of hydrophobicity but much greater rigidity (Supplementary Fig. 11). Under conditions typically used for Pep_b and Pep_c assembly, we found the addition of the hydrophilic tail left the behaviour seen with Pep_b unchanged. Disordered clusters did not form, and the pathway was direct (Supplementary Fig. 12). In contrast, as with Pep_c , addition of the rigid hydrophobic tail of Pep_r led to cluster

Table 1 | Pep_b - Pep_b and Pep_b -mica binding free energy versus Ca^{2+} concentration as determined by DFS.

C_{Ca} (mM)	$\Delta G_{\text{Pep}_b\text{-Pep}_b}$ (kT)	$\Delta G_{\text{Pep}_b\text{-mica}}$ (kT)
5	-4.98 ± 0.08	-3.39 ± 0.55
10	-3.55 ± 0.37	-5.13 ± 1.3
20	-2.08 ± 0.07	-5.35 ± 1.37

formation, and these again served as precursors to crystallization (Supplementary Fig. 13). Taken together, these results demonstrate that creation of disordered precursor clusters is a consequence of the hydrophobicity of the conjugated tail.

Given the poor temporal resolution of conventional AFM, an argument could be made that even Pep_b precipitates start out as disordered clusters, but convert to bilayer crystals too quickly to be observed. We examined Pep_b crystallization using high-speed AFM with a frame rate approximately 125 times greater than for conventional imaging (Methods). Although we observed highly

transient monomeric or small oligomeric adsorbates a few Å in height, which appeared and disappeared in a single frame, as before, 5-Å-high clusters were not observed and Pep_b crystals formed directly (Supplementary Fig. 14). Although the possibility remains that, at very short times, inherent thermal fluctuations of the system that underlie all nucleation processes produce disordered clusters even for Pep_b , we distinguish these from the long-lived disordered precursors that characterize two-step pathways, such as those seen with Pep_c .

Discussion

The findings reported above have a number of implications for understanding crystallization pathways. The behaviour of Pep_b shows that, even for slightly complex molecules, simple pathways can dominate. However, Pep_c crystallization demonstrates that slight alterations in sequence can switch the pathway from simple to two-step. Moreover, the propensity for monomers to aggregate can significantly influence their tendency towards this switch.

Because Pep_c crystals form via conformational transformation of initial clusters, which form spontaneously (probably as a micellar pseudophase), conventional expressions of classical nucleation theory (CNT) do not describe the kinetics. Instead, rates are determined by cluster number densities along with rate constants for cluster transformation into crystalline particles, as described by the coupled differential equations in our model.

Pep_b crystal formation does display a number of the features characteristic of nucleation including: concentration-dependent incubation times (Fig. 3d); a linear dependence of crystal growth rate v on C_p (Supplementary Fig. 15a), implying growth units are monomers; and a dependence of J on supersaturation σ that is fitted well by the expressions of CNT (Supplementary Fig. 15b), and gives a reasonable interfacial free energy ($3.3 \times 10^{-2} \text{ J m}^{-2}$) lying between the values for proteins ($\sim 1 \times 10^{-3} \text{ J m}^{-2}$) and low-solubility inorganic crystals ($\sim 1 \times 10^{-1} \text{ J m}^{-2}$)²¹. However, the rate data can also be interpreted as evidence for barrier-free phase separation in which disordered clusters are akin to the pre-nucleation clusters proposed for certain inorganic systems^{9,22} and formation rates are a reflection of kinetic barriers to transformation. A power-law fit to J versus C_p , which gives an exponent of ~ 4 (Supplementary Fig. 15c), then implies the fundamental growth unit is a tetramer. However, because the linear dependence of growth rate on concentration implies the growth unit is monomeric (Supplementary Fig. 15a), for both to be correct the fundamental unit associated with formation of Pep_b crystals would have to be distinct from that associated with subsequent growth.

Whereas the two-step process observed here is distinct from those in which bulk disordered phases precede nucleation^{10,23}, the relation to systems exhibiting disordered microscopic precursors is less clear. In the mechanism proposed for proteins^{4,7}, crystals form within microscopic dense liquid droplets that share similarities to Pep_c precursors, in that misfolded protein monomers or oligomers are thought to be the constituents and hydrophobicity drives their formation^{24,25}. The similarity of the crystallization step is less clear; a very small fraction of the proteins within a droplet appear to form the crystal nucleus^{4,7,24,25}, whereas, given the size of Pep_c clusters, most of the peptoids seem to comprise the nucleus. The relationship of Pep_c clusters to pre-nucleation clusters (PNCs) reported for inorganic systems^{9,26} is similarly unclear. PNCs are proposed to form spontaneously, but as loose polymeric chains. Moreover, how PNCs transition to crystals and whether that process reflects classical nucleation or aggregation and reaction kinetics is unknown. Thus defining the relationships between various two-step processes remains an open challenge.

Finally, because the ability to produce and isolate disordered precursors or proceed directly to a crystalline phase is of potential value both in living systems^{27,28} and synthetic processes, such as drug

formulation^{8,29}, these insights suggest a valuable design principle: pathway selection can be achieved by tuning the magnitude of the free energy of oligomerization, which governs the likelihood of forming precursors to crystallization.

Methods

Methods, including statements of data availability and any associated accession codes and references, are available in the [online version of this paper](#).

Received 20 February 2016; accepted 9 March 2017;
published online 17 April 2017

References

- Kashchiev, D. Thermodynamically consistent description of the work to form a nucleus of any size. *J. Chem. Phys.* **118**, 1837–1851 (2003).
- Chung, S., Shin, S. H., Bertozzi, C. R. & De Yoreo, J. J. Self-catalyzed growth of S layers via an amorphous-to-crystalline transition limited by folding kinetics. *Proc. Natl Acad. Sci. USA* **107**, 16536–16541 (2010).
- De Yoreo, J. J. *et al.* Crystallization by particle attachment in synthetic, biogenic, and geologic environments. *Science* **349**, aaa6760 (2015).
- Galkin, O., Chen, K., Nagel, R. L., Hirsch, R. E. & Vekilov, P. G. Liquid–liquid separation in solutions of normal and sickle cell hemoglobin. *Proc. Natl Acad. Sci. USA* **99**, 8479–8483 (2002).
- Nielsen, M. H., Aloni, S. & De Yoreo, J. J. *In situ* TEM imaging of CaCO_3 nucleation reveals coexistence of direct and indirect pathways. *Science* **345**, 1158–1162 (2014).
- Smith, B. J. & Dichtel, W. R. Mechanistic studies of two-dimensional covalent organic frameworks rapidly polymerized from initially homogenous conditions. *J. Am. Chem. Soc.* **136**, 8783–8789 (2014).
- Vekilov, P. G. Two-step mechanism for the nucleation of crystals from solution. *J. Cryst. Growth* **275**, 65–76 (2005).
- Erdemir, D., Lee, A. Y. & Myerson, A. S. Nucleation of crystals from solution: classical and two-step models. *Acc. Chem. Res.* **42**, 621–629 (2009).
- Gebauer, D. & Colfen, H. Prenucleation clusters and non-classical nucleation. *Nano Today* **6**, 564–584 (2011).
- Wallace, A. F. *et al.* Microscopic evidence for liquid–liquid separation in supersaturated CaCO_3 solutions. *Science* **341**, 885–889 (2013).
- Savage, J. & Dinsmore, A. Experimental evidence for two-step nucleation in colloidal crystallization. *Phys. Rev. Lett.* **102**, 198302 (2009).
- Sun, J. & Zuckermann, R. N. Peptoid polymers: a highly designable bioinspired material. *ACS Nano* **7**, 4715–4732 (2013).
- Nam, K. T. *et al.* Free-floating ultrathin two-dimensional crystals from sequence-specific peptoid polymers. *Nat. Mater.* **9**, 454–460 (2010).
- Mannige, R. V. *et al.* Peptoid nanosheets exhibit a new secondary-structure motif. *Nature* **526**, 415–420 (2015).
- Chen, C.-L., Zuckermann, R. N. & De Yoreo, J. J. Surface-directed assembly of sequence-defined synthetic polymers into networks of hexagonally-patterned nanoribbons with controllable functionalities. *ACS Nano* **10**, 5314–5320 (2016).
- Kühnle, R. I. & Börner, H. G. Calcium ions to remotely control the reversible switching of secondary and quaternary structures in bioconjugates. *Angew. Chem. Int. Ed.* **50**, 4499–4502 (2011).
- Pashley, R. M. & Quirk, J. P. The effect of cation valency on DLVO and hydration forces between macroscopic sheets of muscovite mica in relation to clay swelling. *Colloid Surf.* **9**, 1–17 (1984).
- Xu, L. & Salmeron, M. An XPS and scanning polarization force microscopy study of the exchange and mobility of surface ions on mica. *Langmuir* **14**, 5841–5844 (1998).
- Friddle, R. W., Noy, A. & De Yoreo, J. J. Interpreting the widespread nonlinear force spectra of intermolecular bonds. *Proc. Natl Acad. Sci. USA* **109**, 13573–13578 (2012).
- Friddle, R. W., Podsiadlo, P., Artyukhin, A. B. & Noy, A. Near-equilibrium chemical force microscopy. *J. Phys. Chem. C* **112**, 4986–4990 (2008).
- De Yoreo, J. J. & Vekilov, P. G. in *Biomimetalization Vol. 54 Reviews in Mineralogy Geochemistry* (eds Dove, P. M., De Yoreo, J. J. & Weiner, S.) 57–93 (Mineralogical Society of America, 2003).
- De Yoreo, J. Crystal nucleation: more than one pathway. *Nat. Mater.* **12**, 284–285 (2013).
- Pouget, E. M. *et al.* The initial stages of template-controlled CaCO_3 formation revealed by Cryo-TEM. *Science* **323**, 1455–1458 (2009).
- Byington, M. C., Safari, M. S., Conrad, J. C. & Vekilov, P. G. Protein conformational flexibility enables the formation of dense liquid clusters: tests using solution shear. *J. Phys. Chem. Lett.* **7**, 2339–2345 (2016).

25. Vorontsova, M. A., Chan, H. Y., Lubchenko, V. & Vekilov, P. G. Lack of dependence of the sizes of the mesoscopic protein clusters on electrostatics. *Biophys. J.* **109**, 1959–1968 (2015).
26. Gebauer, D., Volkel, A. & Colfen, H. Stable prenucleation calcium carbonate clusters. *Science* **322**, 1819–1822 (2008).
27. Addadi, L., Raz, S. & Weiner, S. Taking advantage of disorder: amorphous calcium carbonate and its roles in biomineralization. *Adv. Mater.* **15**, 959–970 (2003).
28. Gal, A., Weiner, S. & Addadi, L. A perspective on underlying crystal growth mechanisms in biomineralization: solution mediated growth versus nanosphere particle accretion. *CrystEngComm* **17**, 2606–2615 (2015).
29. Du, W., Cruz-Cabeza, A. J., Woutersen, S., Davey, R. J. & Yin, Q. Can the study of self-assembly in solution lead to a good model for the nucleation pathway? The case of tolafenamic acid. *Chem. Sci.* **6**, 3515–3524 (2015).

Acknowledgements

Peptoid synthesis, MD simulations, *in situ* AFM, DFS and TEM characterization and high-speed AFM imaging were supported by the US Department of Energy, Office of Basic Energy Sciences, Biomolecular Materials Program at Pacific Northwest National Laboratory (PNNL) and the Lawrence Livermore National Laboratory. Development of MD potentials and peptoid designs was supported by the Materials Synthesis and Simulation Across Scales Initiative through the LDRD Program at PNNL. PNNL is a multi-program national laboratory operated for Department of Energy by Battelle under

Contract No. DE-AC05-76RL01830. Work at the Lawrence Livermore National Laboratory was performed under the auspices of the US Department of Energy under Contract DE-AC52-07NA27344.

Author contributions

X.M. performed AFM and DLS experiments, data analysis and manuscript writing; S.Z. performed AFM experiments, data analysis and manuscript writing; F.J. performed DFS measurements; C.J.N. performed cryoTEM imaging; Y.Z. performed high-speed AFM imaging; A.P. performed MD simulations; Z.L. performed peptoid synthesis and characterization; M.D.B. performed MD simulations and manuscript writing; C.J.M. designed the simulations; J.P. designed the simulations; A.N. designed the high-speed AFM experiments and performed manuscript writing; C.-L.C. designed the study and performed peptoid design, synthesis and characterization, and manuscript writing; J.J.D.Y. designed the study, developed and applied the mathematical model, and performed data analysis and manuscript writing.

Additional information

Supplementary information is available in the [online version of the paper](#). Reprints and permissions information is available online at www.nature.com/reprints. Publisher's note: Springer Nature remains neutral with regard to jurisdictional claims in published maps and institutional affiliations. Correspondence and requests for materials should be addressed to C.-L.C. or J.J.D.Y.

Competing financial interests

The authors declare no competing financial interests.

Methods

Peptoid synthesis. Peptoids were synthesized using a modified solid-phase submonomer synthesis method as described previously³⁰ and detailed in the Supplementary Methods, part I. They were either synthesized on a commercial Aapptec Apex 396 robotic synthesizer or manually synthesized in a 6.0 ml plastic vial. Peptoids were cleaved from the resin by addition of 95% trifluoroacetic acid (TFA) in water, and then dissolved in water and acetonitrile (v/v = 1:1) for high-performance liquid chromatography purification.

Preparation of peptoid stock solution. Lyophilized peptoids (3.0×10^{-6} mol) were mixed with 1.5 ml in deionized ($\geq 18 \text{ M}\Omega$) and filtered (0.2 μm) water in a glass vial, and 10 μl 2.0 M aqueous NaOH solutions were used to facilitate dissolution. The final concentration of peptoid stock solution was 2.0 mM.

AFM imaging. All *in situ* images were collected using oxide-sharpened silicon nitride probes (PNP-TR, $k = 0.32 \text{ N m}^{-1}$, and tip radius $< 10 \text{ nm}$; NanoWorld) in semi-contact mode with a Nanoscope VIII (Bruker) inside an enclosed fluid cell at room temperature. *In situ* AFM samples were prepared by directly mixing CaCl_2 solutions with the stock peptoid solution in a plastic vial to reach desired concentrations, and then injecting into the fluid cell on freshly cleaved mica. *Ex situ* images were collected using silicon probes (AC160TS and tip radius of 9 nm; Olympus) in semi-contact mode with a Cypher AFM (Asylum Research) at room temperature. Images were analysed using Nanoscope Analysis v1.4 (Bruker). At least two replicate experiments were performed for each Ca^{2+} /peptoid concentration condition, except for the one labelled 10 mM Ca^{2+} , 0.2 mM Pep_6 .

High-speed (HS)-AFM imaging. HS-AFM images of Pep_6 assembly were collected in tapping mode using a dedicated HS-AFM instrument (RIBM) and high-density carbon/diamond-like carbon (HDC/DLC) ultra-short probes (USC-F1.2-k0.15, NanoWorld, tip radius $< 10 \text{ nm}$). The experimental procedure was similar to the procedure used for conventional AFM imaging. Briefly, the Pep_6 sample from stock solution was premixed with 10 mM CaCl_2 to get the final concentration of 0.1 mM, and immediately injected to the fluid cell for imaging. The approximate time delay between the solution injection and the start of the imaging (due to the cantilever approach procedure) was about 2 min. In a typical experiment we collected 128×128 pixel images from a $300 \text{ nm} \times 300 \text{ nm}$ area at a scan rate of 1 frame per second. Images were analysed with IgorPro and ImageJ software packages.

Dynamic force spectroscopy (DFS). DFS measurements were done using gold-coated silicon nitride probes (OBL and $k = 0.03 \text{ N m}^{-1}$; Bruker) in contact mode with a Cypher AFM (Asylum Research). Details of the tip cleaning and crosslinking, force measurement and data analysis are provided elsewhere^{19,31}. The

mean rupture forces were plotted versus the loading (that is, tip retraction) rate. The fit of these data using the multi-bond model¹⁹ gave the single-molecule free energies for peptoid–mica and peptoid–peptoid binding. Measurements were performed for Pep_6 only, because the hydrophobic tail on Pep_6 precluded peptoid functionalization of the AFM tip. However, because Ca –carboxylate coordination is the source of Ca –peptoid interaction, the behaviour of Pep_6 should also be similar to that of Pep_6 , as illustrated by the fact that both peptoids exhibit similar increases in adsorption rate with increasing C_{Ca} .

Dynamic light scattering (DLS). DLS was performed using a zeta potential analyser (Brookhaven Instruments) at 22°C for solutions prepared using the same procedures as for the AFM studies.

TEM characterization. TEM samples were prepared by pipetting one drop of either freshly made or 1 h-incubated peptoid solution (0.1 mM peptoid and 10 mM CaCl_2) onto 300 mesh copper TEM grids with a carbon film support (Electron Microscopy Sciences) and allowed to dry at ambient temperature. For enhanced contrast, 2% phosphotungstic acid was used as a negative stain. Microscopy was performed on a Tecnai (FEI) operating at 200 kV and images were collected using an Eagle (FEI) bottom mounted camera. For cryogenic TEM, plunge freezing of samples was done using an FEI Vitrobot (Mark III, FEI) and imaged with an FEI Tecnai T-12 fitted with a LaB6 filament operating at an accelerating voltage of 120 kV. A small volume (4–5 μl) of peptoid solution was deposited on a 300 mesh copper TEM grid with a lacey carbon support film (Electron Microscopy Sciences Hatfield) in a humidified chamber. The excess volume was then blotted with filter paper and the sample was plunge frozen into a reservoir of liquid ethane, which was cooled by liquid nitrogen. The sample was then transferred to a Gatan 626 cryogenic holder under liquid nitrogen and inserted into the microscope, where the sample was maintained at -175°C or below. Images were collected using a Gatan $2 \times 2 \text{ K}$ Ultrascan 1000 charge-coupled device with a ‘U’ scintillator using Gatan Digital micrograph software.

Data availability. The authors declare that the data supporting the findings of this study are available within the paper and its supplementary information files.

References

- Zuckermann, R. N., Kerr, J. M., Kent, S. B. H. & Moos, W. H. Efficient method for the preparation of peptoids [oligo(N-substituted glycines)] by submonomer solid-phase synthesis. *J. Am. Chem. Soc.* **114**, 10646–10647 (1992).
- Friddle, R. W. *et al.* Single-molecule determination of the face-specific adsorption of Amelogenin's C-terminus on hydroxyapatite. *Angew. Chem. Int. Ed.* **50**, 7541–7545 (2011).